

Artificial Intelligence Guided Studies of van der Waals Magnets

Trevor David Rhone,* Romakanta Bhattarai, Haralambos Gavras, Bethany Lusch, Misha Salim, Marios Mattheakis, Daniel T. Larson, Yoshiharu Krockenberger, and Efthimios Kaxiras

A materials informatics framework to explore a large number of candidate van der Waals (vdW) materials is developed. In particular, in this study a large space of monolayer transition metal halides is investigated by combining high-throughput density functional theory calculations and artificial intelligence (AI) to accelerate the discovery of stable materials and the prediction of their magnetic properties. The formation energy is used as a proxy for chemical stability. Semi-supervised learning is harnessed to mitigate the challenges of sparsely labeled materials data in order to improve the performance of AI models. This approach creates avenues for the rapid discovery of chemically stable vdW magnets by leveraging the ability of AI to recognize patterns in data, to learn mathematical representations of materials from data and to predict materials properties. Using this approach, previously unexplored vdW magnetic materials with potential applications in data storage and spintronics are identified.

of interesting properties including superconductivity, topological insulating behavior, and magnetic order.^[1] There is an exigent need to identify 2D materials with properties suitable for advances in science and technological innovation. Traditional tools for materials discovery, based on serial experiments or first-principles calculations, are slow and expensive. Identifying a means of accelerating the discovery process for materials with exotic electronic spin and charge degrees of freedom is an active area of research.^[2–10] In addition, a general approach to design a crystal structure with any desired property, although of great scientific interest and practical importance, is still in the early stages of development.^[11–13] The work described here advances the design of novel vdW magnets.

Long-range magnetic ordering in 2D crystals has recently been discovered,^[14,15] leading to a race to better understand the properties of magnetism in reduced dimensions and to identify additional 2D magnets with desirable properties for applications in spintronics and data storage.^[16–19] Since long-range magnetic order can be strongly suppressed in 2D according to the Mermin–Wagner theorem,^[20] 2D crystals, such as monolayer CrI₃, provide a new platform for exploring the interplay between reduced dimensionality and magnetocrystalline anisotropy (MCA). MCA stabilizes magnetic ordering in 2D materials. This interplay could give rise to spin degrees of freedom such as spin textures, that have both scientific interest and relevance for developing novel quantum computing architectures.

1. Introduction

1.1. Magnetic Ordering in Reduced Dimensions

Two-dimensional (2D) materials, also referred to as van der Waals (vdW) materials due to the weak interlayer forces, exhibit a range

T. D. Rhone, R. Bhattarai, H. Gavras

Department of Physics
Applied Physics and Astronomy
Rensselaer Polytechnic Institute
110 8th Street, Troy, NY 12180, USA
E-mail: rhonet@rpi.edu

B. Lusch, M. Salim

Argonne Leadership Computing Facility
Argonne National Laboratory
9700 S. Cass Avenue, Lemont, IL 60439, USA

M. Mattheakis, D. T. Larson, E. Kaxiras
Department of Physics
Harvard University
17 Oxford St, Cambridge, MA 02138, USA

Y. Krockenberger
NTT Basic Research Laboratories
NTT Corporation
3-1 Morinosato-Wakamiya, Atsugi, Kanagawa 243-0198, Japan

The ORCID identification number(s) for the author(s) of this article can be found under <https://doi.org/10.1002/adts.202300019>

DOI: 10.1002/adts.202300019

1.2. Layered Transition Metal Halides

2D vdW ferromagnets have been identified in five structurally distinct groups, namely, transition metal phosphorous trichalcogenides, transition metal halides, ternary iron-based tellurides, transition metal oxyhalides, and transition metal dichalcogenides.^[1,21] In this study we focus on the family of transition metal halides (see **Figure 1**). This class of 2D solids includes materials with different stoichiometries and crystal phases.^[22] They are mainly composed of dihalides MX₂ and trihalides MX₃ (M = V, Cr, Mn, Fe, Co, Ni, Ru; X = Cl, Br, I). Due to the relatively large atomic radius of halide anions and

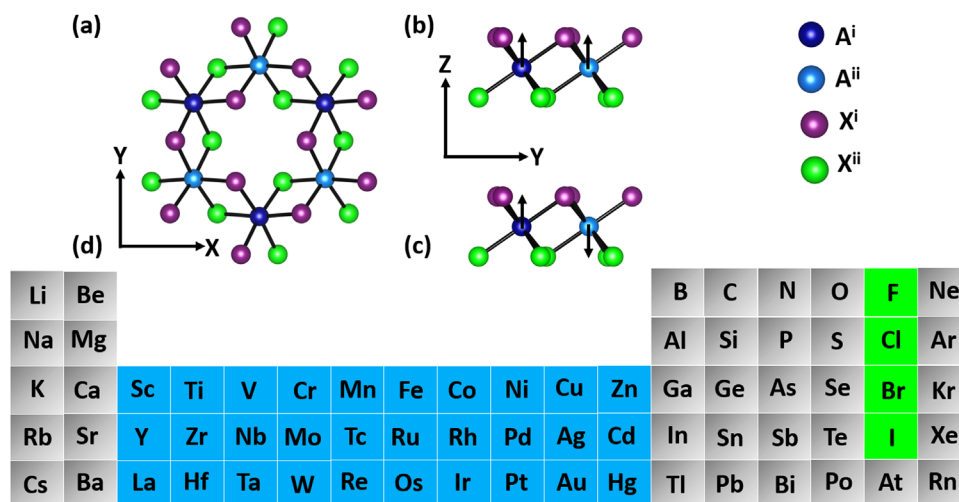


Figure 1. a) The crystal structure of the family of transition metal halides A_2X_6 , based on Cr_2I_6 , used in this study. One or both A sites are replaced with transition metal atoms (highlighted blue in the periodic table in panel (d)) and the X-sites (above and/or below) the plane are replaced with halogens (highlighted green). The magnetic configurations studied are b) ferromagnetic and c) antiferromagnetic. d) The elements used to make chemical substitutions are highlighted in the periodic table.

the partially filled 3d electronic shells of transition metal cations, magnetic vdW materials with a layered structure are expected to emerge from these compounds.^[22] For many years, electronic correlations in Cr trihalides have been investigated, and a series of exciting phenomena were revealed in this family of materials. Cr trihalides with different anions exhibit different properties. These include: a) The intralayer exchange of these three compounds is ferromagnetic (FM), while the interlayer exchange changes from antiferromagnetic (AFM) to FM (from $CrCl_3$ to $CrBr_3$). The magnetic order for CrI_3 depends on the layer number. The corresponding magnetization direction varies from in-plane ($CrCl_3$) to out-of-plane ($CrBr_3$ and CrI_3).^[23] b) Owing to the governing superexchange interaction^[24] and spin-orbit coupling (SOC),^[24] the Curie temperature T_C of several layers of Cr trihalides increases from 17 K ($CrCl_3$) to 37 K ($CrBr_3$) then to 46 K (CrI_3);^[23] this trend stems from the extended anion radius and as well as higher atomic number. c) The spin models that describe 2D magnetism are the XY and Ising models for $CrCl_3$ and CrI_3 , respectively. The description of $CrBr_3$ lies between the Heisenberg and Ising models,^[25] indicating the importance of exchange anisotropy linked to the increase of the atomic number of the halide anion. In addition, the spin-flip field decreases with the increasing temperature in CrI_3 and $CrCl_3$.^[26] The T_C of $CrBr_3$ and $CrCl_3$ increases as the magnetic field increases, while it is almost field-independent in CrI_3 due to the large anisotropy. In addition, various phenomena such as large valley splitting,^[27] higher-spin Kitaev model,^[28] and quantum anomalous Hall effect,^[29] have been reported in transition metal halides, suggesting their potential in different research fields.

Monolayer CrX_3 has a hexagonal lattice with point group D_{3d} .^[30] The present study will use this crystal structure as the prototype structure and explore how changes in chemical composition affect its magnetic and thermodynamic properties. A more thorough investigation of competing phases is left for future work.

1.3. Materials Discovery Using AI

Materials data (created from experiments or from first-principles calculations) combined with AI can be used to accelerate materials science research and discovery.^[9,31–33] AI models trained on a set of crystal structures and corresponding material properties can predict the properties of a much larger space of materials. In particular, there is a great deal of interest in harnessing AI for identifying novel magnetic materials.^[8,9] Recent studies leveraging AI to study materials highlight the importance of the careful choice of descriptors for making successful predictions.^[32,34] In these studies, state-of-the-art mathematical representations of crystal structures, based on graph neural networks, were constructed to reliably model material properties.

Early efforts to create materials descriptors used chemical composition only^[9,35] and later incorporated simple metrics for encoding crystal structure.^[36,37] Recent studies demonstrate that AI models constructed from descriptors using chemical compositions can be successful if the study is restricted to isostructural materials.^[9] Another recent approach of increasing interest is to create mathematical representations of materials from data.^[32] AI models (neural networks in particular) are universal function approximators that contain increasingly sophisticated representations in successive hidden layers of the neural network. In the case of the neural network autoencoder architecture, a compressed representation of the data is created in the embedding layer, or latent space of the autoencoder. This gives rise to the prospect of using AI to uncover physical insight through the study of the latent space representation by linking the encoded representation of a material to its target property. The autoencoder's latent space can conceivably elucidate patterns in a high-dimensional descriptor space revealing relationships that lead to physical insight.^[38]

A major challenge in materials informatics is the scant amount of data, or more specifically, labeled data that can be used for supervised learning. To overcome this challenge, efforts have been

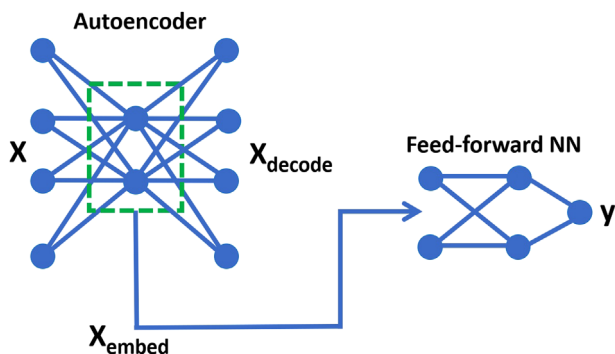


Figure 2. The neural network architecture used to implement semi-supervised learning. An autoencoder is coupled to a feed-forward neural network. The embedding space of the autoencoder is the input for the feed-forward neural network. The loss functions of the autoencoder and the feed-forward neural network are coupled.

made to perform unsupervised learning, where no labels are needed for inference. In addition, semi-supervised learning can be implemented, where both labeled and unlabeled data are exploited to train models.^[39,40] Although the use of semi-supervised learning has already been reported in the materials discovery literature,^[39,40] this tool appears to be underutilized by the materials informatics community. Semi-supervised learning can be used to mitigate the challenge of scarce data, since increasing the amount of unlabeled data can improve model performance. Since the bottleneck for training AI models is often the lack of difficult to obtain labeled data, semi-supervised learning provides a significant benefit.^[39] In this work, we leverage semi-supervised learning (see **Figure 2**) to overcome the challenge of sparsely labeled data and to search for novel vdW magnets.

Table 1. DFT identifies candidate materials satisfying the search criteria for the formation energy, E_f (eV) and the magnetic moment, μ (μ_B) of CrI_3 . The calculated DFT values for E_f and μ are displayed.

Formula	E_f	μ	Formula	E_f	μ
Cr_2I_6	−6.213	11.3	$\text{Mn}_2\text{Cr}_2\text{Br}_{12}$	−11.082	13.1
MnCrCl_6	−15.767	13.1	$\text{MnTcBr}_3\text{Cl}_3$	−10.971	14.6
$\text{Mn}_2\text{I}_3\text{Cl}_3$	−9.530	15.2	CrFeCl_6	−13.650	14.9
CrFeBr_6	−9.067	14.8	$\text{MnReI}_3\text{Cl}_3$	−6.488	14.1
$\text{CrFeI}_3\text{Cl}_3$	−8.210	14.4	$\text{CrFeBr}_3\text{Cl}_3$	−11.307	14.9
$\text{Fe}_2\text{Br}_3\text{Cl}_3$	−8.102	18.5			

2. Results and Discussion

A subset of the density functional theory (DFT) results are shown in **Figure 3**. The displayed results constitute the ground state magnetic configuration, with the formation energy, E_f on the left and the magnetic moment, μ on the right. Calculations were performed on 700 candidates out of a total of $\approx 10^4$ candidates. The gray squares represent the combinations that were not calculated. The magnetic moment and formation energy values vary with changes in chemical composition. The objective in this work is to identify materials with large magnetic moments that are also chemically stable as determined by their formation energy. For instance, we highlight that our DFT search finds that several A_2X_6 structures have magnetic moments larger than that of CrI_3 , with formation energy lower (hence more stable) than that of CrI_3 (see **Table 1**).

Next, we train a neural network (NN) model to learn the relationship between a crystal structure's chemical composition and its corresponding magnetic and thermodynamic properties.

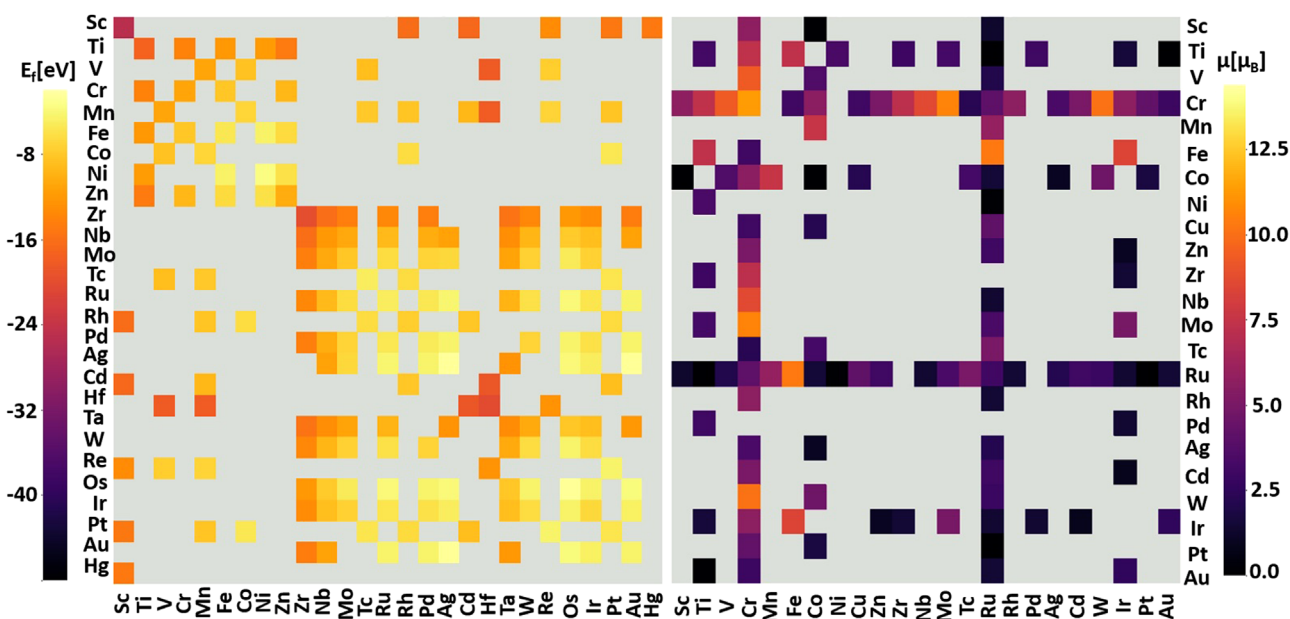


Figure 3. A subset of the DFT results are displayed. The left panel shows the formation energy, E_f (eV) for $\text{A}^i \text{A}^{ii} \text{X}_3^{ij}$ candidates where $\text{X}^i \text{X}^{ii} = \text{Br}_3 \text{Cl}_3$. The right panel shows the magnetic moment, μ (μ_B) for $\text{A}^i \text{A}^{ii} \text{X}_3^{ij}$ candidates where $\text{X}^i \text{X}^{ii} = \text{I}_3 \text{I}_3$. The horizontal axis shows the A^i sites and the vertical axis shows the A^{ii} sites. Candidates that were not calculated are represented by gray squares.

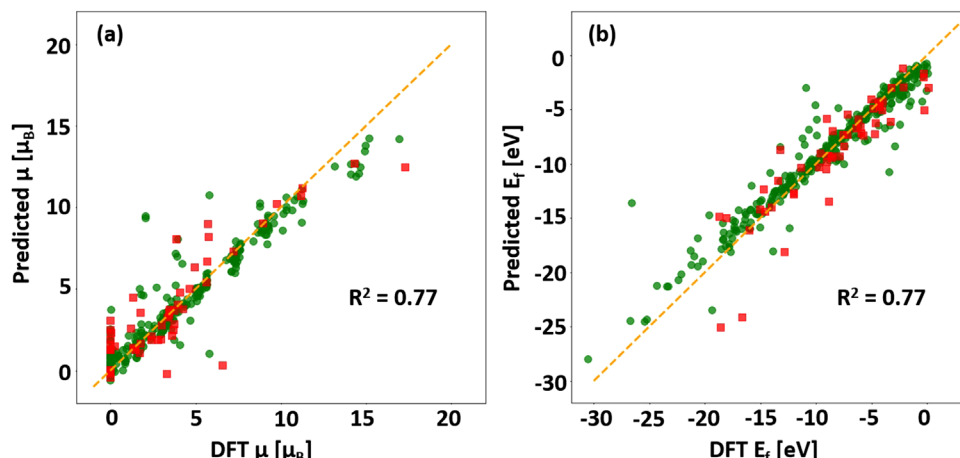


Figure 4. The parity plot for the AI results are shown for a) magnetic moment μ (μ_B) and b) formation energy E_f (eV). The test set R^2 score is 0.77. The red squares (green circles) indicate test (training) set data.

Training was performed with both labeled and unlabeled data using semi-supervised learning. The trained NN facilitates the fast and accurate prediction of materials properties for the entire materials space, allowing us to quickly identify materials candidates that might satisfy our search criteria. The NN model performance is displayed in **Figure 4** for both the magnetic moment and the formation energy. The parity plots show good model performance for both the magnetic moment and the formation energy. We note that the training tasks for the magnetic moment and the formation energy were coupled together and not trained independently using two separate models. An additional training task, the magnetic excitation energy, ΔE , was added to the model's loss function to further constrain the NN. By adding the magnetic excitation energy and the formation energy to the loss function for the magnetic moment prediction, we incorporate soft constraints into the NN. This is an example of physics informed machine learning (PIML), a state-of-the-art approach at the intersection of physics and AI.^[41–44] Our PIML approach links the magnetic excitation energy to the physics of the system by mapping the DFT energies to the Heisenberg spin Hamiltonian^[45] as shown in Equation (1)

$$\begin{aligned} E_{\text{FM}} &= E_0 + (3J_1 + 6J_2 + 3J_3)|\vec{S}|^2 \\ E_{\text{AFM}} &= E_0 + (-3J_1 + 6J_2 - 3J_3)|\vec{S}|^2 \\ \Delta E &= E_{\text{FM}} - E_{\text{AFM}} \\ &= 6(J_1 + J_3)|\vec{S}|^2 \end{aligned} \quad (1)$$

The magnetic excitation energy is the difference in the DFT total energy of the ferromagnetic configurations, E_{FM} and the antiferromagnetic configurations, E_{AFM} . ΔE is determined by J_1 and J_3 (see Equation (1)), where J_1 , J_2 , and J_3 are the first, second, and third nearest neighbor interactions, respectively. \vec{S} represents the spin on the transition metal atom.

If we require the model to learn ΔE , E_f , and μ simultaneously, we can better constrain the NN model. We find that this soft con-

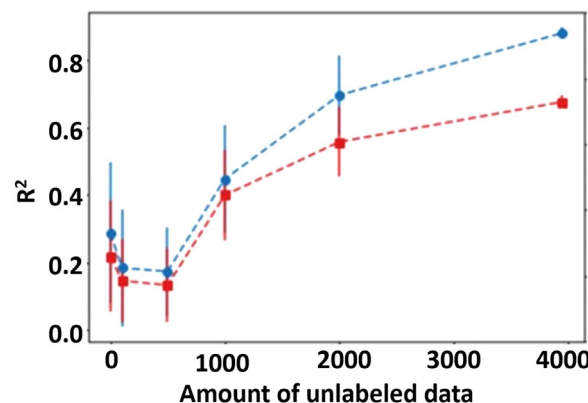


Figure 5. The R^2 validation set score versus the number of unlabeled data points is displayed. Increasing the amount of unlabeled data in our semi-supervised learning tasks improves the prediction performance. Markers delimit the mean R^2 score and errors bars indicate the standard deviation of these scores for a set of ten separate runs. The red squares (blue circles) indicate test (training) set data.

straint decreases overfitting when compared with a model trained with only μ in the loss function.

To demonstrate the usefulness of the semi-supervised learning approach we trained several models with varying amounts of unlabeled data. Increasing the amount of unlabeled data increased the NN model performance as shown in **Figure 5**. With about 700 labeled data points and no unlabeled data we obtained an average R^2 validation score of 0.2. With only additional unlabeled data points (up to 4000) we get an increase in the R^2 to 0.8. The NN performance improves with increased amounts of unlabeled data due to the autoencoder portion of the NN becoming better at learning the materials representation. The FNN is then better able to make predictions given the improved inputs created by the latent space of the autoencoder.^[46]

In addition, we compared our semi-supervised learning NN with a baseline model. We used linear regression, a standard model for regression tasks, to assess the performance of the proposed deep learning model. We found that the semi-supervised

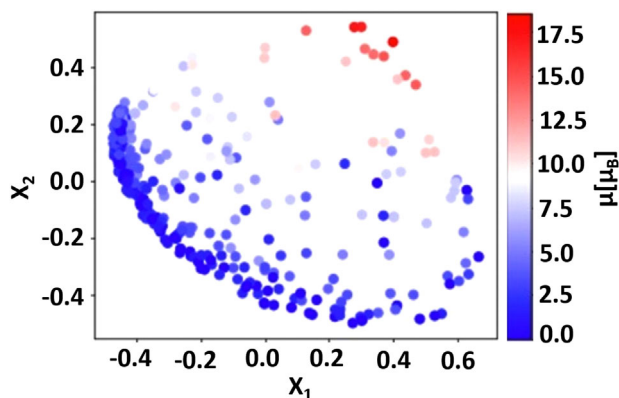


Figure 6. The 2D projection of the embedding space of the autoencoder neural network is displayed. The first and second principal components, X_1 and X_2 , are on the horizontal and vertical axis, respectively. A pattern in the data emerges indicating a connection between the position in embedding space and the value of the magnetic moment.

learning NN model greatly outperforms the linear regression model, which resulted in overfitting and poor test score performance. Additional details on the linear regression model and its performance are included in the Supporting Information.

We attempt to extract physical insight from the autoencoder NN by analyzing the latent space. Using principal component analysis (PCA) we project the latent space onto the first two principal components, X_1 , X_2 and plot the results in **Figure 6**. A pattern emerges in the 2D projection of the latent space where materials with small magnetic moment are in one region while materials with larger magnetic moments are in another part of the 2D latent space. This suggests that there is a link between crystal structure and chemical composition, as encoded using the smooth overlap of atomic positions (SOAP) descriptor^[54], and the magnetic moment. A recent study using a crystal diffusion variational autoencoder^[47] further highlights the benefit of using autoencoders to create a latent space. In particular, the study leveraged the latent space of an autoencoder to generate crystal structures with desirable properties.

The NN can be used to rapidly predict the properties of candidate materials and to screen for those materials with large magnetic moment and high chemical stability. We compared the AI predictions with the labeled data in the validation/training set; of the 496 predictions, 14 satisfied the following search criterion: magnetic moment $\mu > 11.3 \mu_B$ and formation energy $E_f < -6.213$ eV. Examples of the promising candidates include: $Mn_4I_6Cl_6$, $Cr_2Fe_2Cl_{12}$, and $Mn_2Cr_2Br_{12}$. The candidates and their corresponding properties are displayed in **Table 2**. Although the formation energy is a proxy for chemical stability, it is a necessary but not sufficient indicator for chemical stability. Additional criteria for chemical stability include tests for: i) the dynamic stability and ii) the presence of competing phases. The dynamic stability is demonstrated by the absence of imaginary phonon modes. Competing phases can be investigated by calculating the energy above convex hull.^[47,48] Although, metastable phases, that is, phases above the convex hull, may exist in nature.^[49,50] We calculated the phonon dispersion for the following promising structures: $Cr_2Fe_2Br_6Cl_6$, $Fe_2Cr_2Br_{12}$, $Mn_2Cr_2Cl_{12}$, and $Mn_4I_6Cl_6$ and found that they were dynamically stable except for $Mn_4I_6Cl_6$ (see

Table 2. Materials candidates that satisfy the search criteria (i.e., higher magnetic moment and lower formation energy than that of Cr_2I_6) are displayed alongside the formation energy, E_f (eV) and the magnetic moment, μ (μ_B) of Cr_2I_6 . The calculated DFT values for E_f and μ are displayed alongside the corresponding AI predicted values. The asterisk indicates those candidates initially chosen from the unlabelled data set.

Formula	E_f (DFT)	E_f (AI)	μ (DFT)	μ (AI)
Cr_2I_6	−6.213	−5.8	9.2	11.3
$MnCrBr_6$	−11.082	−11.2	13.1	11.6
$MnCrCl_6$	−15.767	−14.2	13.1	11.7
$MnReI_3Br_3$	−4.397	−6.4	14.1	12.0
$Fe_2Br_3Cl_3$	−8.102	−12.1	18.5	12.0
$CrFeI_3Br_3$	−6.126	−6.8	14.6	12.4
$MnReI_3Cl_3$	−6.489	−7.1	14.1	12.8
$Fe_2I_3Cl_3$	−5.368	−7.4	16.9	13.2
$MnTcBr_3Cl_3$	−10.971	−9.9	14.6	13.5
$CrFeI_3Cl_3$	−8.210	−7.6	14.4	13.5
$CrFeBr_6$	−9.067	−7.8	14.8	13.7
$CrFeCl_6$	−13.651	−12.0	14.9	13.9
$Mn_2I_3Cl_3$	−9.530	−8.3	15.2	14.2
$CrFeBr_3Cl_3$	−11.307	−9.2	14.9	14.3
* $MnCdBr_3Cl_3$	−11.994	−12.8	5.7	6.7
* $MnVBr_3Cl_3$	−14.713	−12.3	11.2	8.1
* $CrAuCl_6$	−8.898	−9.2	8.9	9.4
* $MoWBr_3Cl_3$	−8.568	−6.9	9.8	9.9
* $MnHgBr_3Cl_3$	−9.121	−10.4	5.7	11.1
* $MnReBr_3Cl_3$	−9.643	−9.1	14.3	13.9

Supporting Information for further details). Calculations of the competing phases, that is, the convex hull, of the materials candidates, although of significance, are beyond the scope of this work.

Furthermore, we chose 71 additional candidates at random from the unlabeled data set, predicted their properties using AI and then chose the six candidates with the highest magnetic moments with $E_f < -6.213$ eV. Additional DFT calculations were used to verify the AI predictions. The resulting promising candidates were $CrAuCl_6$, $MnVBr_3Cl_3$, $MnHgBr_3Cl_3$, $MoWBr_3Cl_3$, $MnReBr_3Cl_3$, and $MnCdBr_3Cl_3$. These results along with their corresponding properties are included in Table 2.

The distribution of values for the AI predictions of the magnetic moment and the formation energy were compared with the distribution of those quantities obtained using DFT. We find that the distributions for both, formation energy and magnetic moment, are similar. A histogram of the magnetic moment and the formation energy for both the AI predictions and the DFT results can be found in the Supporting Information.

We inspected the results in Table 2, which highlights the materials with the largest magnetic moment that have formation energy, $E_f < -6.123$ eV. We find that many of the structures comprise elements from Groups 6 or 7 of the periodic table at one or both A sites. This is consistent with these elements yielding a large local magnetic moment at the A sites; the maximum total magnetic moment resulting from the sum of the local magnetic moments.

3. Conclusion

We created a machine learning framework leveraging semi-supervised learning to accelerate the discovery of monolayers of transition metal halides. Semi-supervised learning mitigates the lack of labeled data by creating a mathematical representation of the materials using unlabeled data. Furthermore, we identified novel transition metal halides with large magnetic moments that are predicted to be chemically stable as evidenced by the thermodynamic and dynamic stability calculations. In particular, we predict that $\text{Cr}_2\text{Fe}_2\text{Br}_6\text{Cl}_6$, $\text{Fe}_2\text{Cr}_2\text{Br}_{12}$, and $\text{Mn}_2\text{Cr}_2\text{Cl}_{12}$ are candidate 2D magnetic structures with magnetic moments exceeding those of Cr_2I_6 while minimizing its formation energy. Lower formation energies are key to future developments regarding the discovery of low-dimensional magnetic materials.

Our materials prediction framework can be easily generalized for the exploration of materials with different crystal structures beyond the one considered here. Specifically, different crystal structure prototypes can be used, including mixed ones, for example, a data set comprising both transition metal halides and transition metal trichalcogenides.

4. Experimental Section

Database of First-Principles Calculations: In order to create a framework for investigating 2D magnets using a data-driven approach, a database of crystal structures of the form A_2X_6 , based on monolayer Cr_2I_6 (Figure 1a) was first created using DFT calculations with non-collinear spin and spin-orbit interactions included. There were a combinatorially large number of possible candidate A_2X_6 structures ($\approx 10^4$) with different elements occupying the A and X sites. An initial subset of 700 structures was randomly selected for investigation with DFT (and performed calculations on additional structures at a later stage). The formation energy, magnetic order, and magnetic moment of each crystal structure were obtained. The ground-state properties were determined by examining the energies of the fully optimized structure with several spin configurations, including parallel, and anti-parallel spin orientations at the A sites (Figure 1b). The energy difference between parallel and anti-parallel spin configurations estimated the magnetic excitation energy. The sign of the magnetic excitation energy is an indicator of the magnetic order of a material.

To create the database DFT calculations with the VASP code^[51,52] were used. The GGA-PBE was used for the exchange-correlation functional. The energy cutoff was 450 eV. The vacuum region was thicker than 20 Å. Calculations were performed using 2×1 supercells with two A sites per unit cell. The atoms were fully relaxed until the force on each atom was smaller than $0.01 \text{ eV } \text{\AA}^{-1}$. A Γ -centered $8 \times 8 \times 1$ k -point mesh was utilized. The different structures were created by choosing different transition metal atoms for each of the Cr atoms in the unit cell. The halogens above and below the basal plane were separately selected from F, Br, Cl, or I. Figure 1d shows the choice of substitution atoms in the periodic table. An example of a structure created through this process is $(\text{CrTi})\text{Br}_3\text{Cl}_3$. The FM (AFM) configuration was created by making the spins on the A sites parallel (antiparallel). The magnetic moment per supercell and the formation energy per supercell^[9] were extracted for each relaxed structure and each magnetic configurations. Dynamic stability was estimated by performing phonon calculations using phonopy.^[53] See Supporting Information for additional details on the data set.

Materials Descriptors and AI Modeling: A careful choice of descriptors is essential for the success of any AI approach. Materials descriptors (i.e., mathematical representations of materials) were used for both data analytics and to serve as inputs to AI models. Many materials descriptors had been developed with increasing levels of sophistication, from those based on atomic properties only^[35] to those that incorporate clever

mathematical descriptions of the crystal structure.^[36,37,54] In this study the SOAP kernel was leveraged as a descriptor.^[54] The SOAP kernel encoded chemical composition and crystal structure into a form that could be cast into a vector that was used to describe the position of materials in chemical space. The SOAP kernel was used as an input for the AI models.

Semi-supervised learning was performed using the SOAP kernel as the input and the magnetic moment, the formation energy and the magnetic excitation energy were the target properties. The data were randomly divided into a training/validation set and a test set. Training/validation was typically 90% of the total data while test data comprised 10% of all the data. A combination of NN models to perform semi-supervised learning was employed. That is, an autoencoder was coupled with a feed-forward neural network; the autoencoder neural network (ANN) did not require labels (i.e., unsupervised learning) whereas the feed-forward neural network (FNN) required labels (i.e., supervised learning). See Figure 2 for a schematic of the architecture. The AENN and FNN models were trained at the same time. Successive layers of the autoencoder network facilitated increasingly higher level materials representations. The optimal number of hidden layers and nodes in each hidden layer was found using random hyperparameter search. The embedding layer (i.e., latent space) of the autoencoder was used as the input to the FNN (see the Supporting Information for details on the AI models, including the optimization of hyperparameters). The embedding layer of the ANN learns a representation of the materials data that could be used for pattern recognition when compressed further into a 2D descriptor space. That is, the latent space could be further compressed into two dimensions using PCA or t -distributed stochastic neighbor embedding (t -SNE).^[55,56]

Supporting Information

Supporting Information is available from the Wiley Online Library or from the author.

Acknowledgements

This research was funded in part and used resources of the Argonne Leadership Computing Facility, which is a DOE Office of Science User Facility supported under Contract DE-AC02-06CH11357. Calculations were also performed using the Extreme Science and Engineering Discovery Environment (XSEDE), which is supported by National Science Foundation (Grant number ACI-1548562) and the Odyssey cluster supported by the FAS Division of Science, Research Computing Group at Harvard University. This research was supported by the National Science Foundation CAREER award under Grant No 2044842.

Conflict of Interest

The authors declare no conflict of interest.

Data Availability Statement

The data that support the findings of this study are available from the corresponding author upon reasonable request.

Keywords

2D materials, artificial intelligence, machine learning, magnetic materials, spintronics

Received: January 5, 2023

Revised: March 10, 2023

Published online: April 16, 2023

- [1] Q. H. Wang, A. Bedoya-Pinto, M. Blei, A. H. Dismukes, A. Hamo, S. Jenkins, M. Koperski, Y. Liu, Q.-C. Sun, E. J. Telford, H. H. Kim, M. Augustin, U. Vool, J.-X. Yin, L. H. Li, A. Falin, C. R. Dean, F. Casanova, R. F. L. Evans, M. Chshiev, A. Mishchenko, C. Petrovic, R. He, L. Zhao, A. W. Tsen, B. D. Gerardot, M. Brotons-Gisbert, Z. Guguchia, X. Roy, S. Tongay, et al., *ACS Nano* **2022**, *16*, 6960.
- [2] C. M. Acosta, E. Ogoshi, J. A. Souza, G. M. Dalpian, *ACS Appl. Mater. Interfaces* **2022**, *14*, 9418.
- [3] W. Xia, M. Sakurai, B. Balasubramanian, T. Liao, R. Wang, C. Zhang, H. Sun, K.-M. Ho, J. R. Chelikowsky, D. J. Sellmyer, C.-Z. Wang, *PNAS* **2022**, *119*, e2204485119.
- [4] S. Haastrup, M. Strange, M. Pandey, T. Deilmann, P. S. Schmidt, N. F. Hinsche, M. N. Gjerding, D. Torelli, P. M. Larsen, A. C. Riis-Jensen, J. Gath, K. W. Jacobsen, J. J. Mortensen, T. Olsen, K. S. Thygesen, *2D Mater.* **2018**, *5*, 42002.
- [5] V. Stanev, K. Choudhary, A. G. Kusne, J. Paglione, I. Takeuchi, *Commun. Mater.* **2021**, *2*, 105.
- [6] N. Andrejevic, J. Andrejevic, B. A. Bernevig, N. Regnault, F. Han, G. Fabbri, T. Nguyen, N. C. Drucker, C. H. Rycroft, M. Li, *Adv. Mater.* **2022**, *34*, 2204113.
- [7] H. A. Merker, H. Heiberger, L. Nguyen, T. Liu, Z. Chen, N. Andrejevic, N. C. Drucker, R. Okabe, S. E. Kim, Y. Wang, T. Smidt, M. Li, *iScience* **2022**, *25*, 105192.
- [8] Y. Xie, G. A. Tritsarlis, O. Gr  n  s, T. D. Rhone, *J. Phys. Chem. Lett.* **2021**, *12*, 12048.
- [9] T. D. Rhone, W. Chen, S. Desai, S. B. Torrisi, D. T. Larson, A. Yacoby, E. Kaxiras, *Sci. Rep.* **2020**, *10*, 15795.
- [10] Y. Zhu, X. Kong, T. D. Rhone, H. Guo, *Phys. Rev. Mater.* **2018**, *2*, 81001.
- [11] C.-T. Chen, G. X. Gu, *Adv. Sci.* **2020**, *7*, 1902607.
- [12] A. Zunger, *Nat. Rev. Chem.* **2018**, *2*, 121.
- [13] Z. Ren, S. I. P. Tian, J. Noh, F. Oviedo, G. Xing, J. Li, Q. Liang, R. Zhu, A. G. Aberle, S. Sun, X. Wang, Y. Liu, Q. Li, S. Jayavelu, K. Hippalgaonkar, Y. Jung, T. Buonassisi, *Matter* **2022**, *5*, 314.
- [14] B. Huang, G. Clark, E. Navarro-Moratalla, D. R. Klein, R. Cheng, K. L. Seyler, D. Zhong, E. Schmidgall, M. A. McGuire, D. H. Cobden, W. Yao, D. Xiao, P. Jarillo-Herrero, X. Xu, *Nature* **2017**, *546*, 270.
- [15] C. Gong, L. Li, Z. Li, H. Ji, A. Stern, Y. Xia, T. Cao, W. Bao, C. Wang, Y. Wang, Z. Q. Qiu, R. J. Cava, S. G. Louie, J. Xia, X. Zhang, *Nature* **2017**, *546*, 265.
- [16] N. S. Kiselev, A. N. Bogdanov, R. Sch  fer, U. K. R    ler, *J. Phys. D: Appl. Phys.* **2011**, *44*, 392001.
- [17] W. Han, *APL Mater.* **2016**, *4*, 32401.
- [18] A. Hirohata, K. Yamada, Y. Nakatani, I.-L. Prejbeanu, B. Di  ny, P. Pirro, B. Hillebrands, *J. Magn. Magn. Mater.* **2020**, *509*, 166711.
- [19] H. Y. Yuan, Y. Cao, A. Kamra, R. A. Duine, P. Yan, *Phys. Rep.* **2022**, *965*, 1.
- [20] N. D. Mermin, H. Wagner, *Phys. Rev. Lett.* **1966**, *17*, 1133.
- [21] X. Jiang, Q. Liu, J. Xing, N. Liu, Y. Guo, Z. Liu, J. Zhao, *Appl. Phys. Rev.* **2021**, *8*, 31305.
- [22] M. McGuire, *Crystals* **2017**, *7*, 121.
- [23] H. H. Kim, B. Yang, S. Li, S. Jiang, C. Jin, Z. Tao, G. Nichols, F. Sfigakis, S. Zhong, C. Li, S. Tian, D. G. Cory, G.-X. Miao, J. Shan, K. F. Mak, H. Lei, K. Sun, L. Zhao, A. W. Tsen, *PNAS* **2019**, *116*, 11131.
- [24] D.-H. Kim, K. Kim, K.-T. Ko, J. Seo, J. S. Kim, T.-H. Jang, Y. Kim, J.-Y. Kim, S.-W. Cheong, J.-H. Park, *Phys. Rev. Lett.* **2019**, *122*, 207201.
- [25] C. Jin, Z. Tao, K. Kang, K. Watanabe, T. Taniguchi, K. F. Mak, J. Shan, *Nat. Mater.* **2020**, *19*, 1290.
- [26] H. H. Kim, B. Yang, S. Tian, C. Li, G.-X. Miao, H. Lei, A. W. Tsen, *Nano Lett.* **2019**, *19*, 5739.
- [27] Q. Li, K.-Q. Chen, L.-M. Tang, *Phys. Rev. Appl.* **2020**, *13*, 014064.
- [28] P. P. Stavropoulos, D. Pereira, H.-Y. Kee, *Phys. Rev. Lett.* **2019**, *123*, 037203.
- [29] J. Sun, X. Zhong, W. Cui, J. Shi, J. Hao, M. Xu, Y. Li, *Phys. Chem. Chem. Phys.* **2020**, *22*, 2429.
- [30] M. A. McGuire, H. Dixit, V. R. Cooper, B. C. Sales, *Chem. Mater.* **2015**, *27*, 612.
- [31] F. Mayr, M. Harth, I. Kouroudis, M. Rinderle, A. Gagliardi, *J. Phys. Chem. Lett.* **2022**, *13*, 1940.
- [32] J. Noh, J. Kim, H. S. Stein, B. Sanchez-Lengeling, J. M. Gregoire, A. Aspuru-Guzik, Y. Jung, *Matter* **2019**, *1*, 1370.
- [33] T. Ueno, T. D. Rhone, Z. Hou, T. Mizoguchi, K. Tsuda, *Mater. Discover.* **2016**, *4*, 18.
- [34] R. E. A. Goodall, A. A. Lee, *Nat. Commun.* **2020**, *11*, 6280.
- [35] L. M. Ghiringhelli, J. Vybiral, S. V. Levchenko, C. Draxl, M. Scheffler, *Phys. Rev. Lett.* **2015**, *114*, 105503.
- [36] M. Rupp, A. Tkatchenko, K.-R. M  ller, O. A. von Lilienfeld, *Phys. Rev. Lett.* **2012**, *108*, 58301.
- [37] K. Hansen, F. Biegler, R. Ramakrishnan, W. Pronobis, O. A. von Lilienfeld, K.-R. M  ller, A. Tkatchenko, *J. Phys. Chem. Lett.* **2015**, *6*, 2326.
- [38] F. Oviedo, J. L. Ferres, T. Buonassisi, K. T. Butler, *Acc. Mater. Res.* **2022**, *3*, 597.
- [39] N. C. Frey, J. Wang, G. I. Vega Bellido, B. Anasori, Y. Gogotsi, V. B. Shenoy, *ACS Nano* **2019**, *13*, 3031.
- [40] S. Lolla, H. Liang, A. G. Kusne, I. Takeuchi, W. Ratcliff, *J. Appl. Crystallogr.* **2022**, *55*, 882.
- [41] G. E. Karniadakis, I. G. Kevrekidis, L. Lu, P. Perdikaris, S. Wang, L. Yang, *Nat. Rev. Phys.* **2021**, *3*, 422.
- [42] V. Fung, P. Ganesh, B. G. Sumpter, *Chem. Mater.* **2022**, *34*, 4848.
- [43] M. Mattheakis, D. Sondak, A. S. Dogra, P. Protopapas, *Phys. Rev. E* **2022**, *105*, 6.
- [44] G. P. P. Pun, R. Batra, R. Ramprasad, Y. Mishin, *Nat. Commun.* **2019**, *10*, 2339.
- [45] N. Sivadras, M. W. Daniels, R. H. Swendsen, S. Okamoto, D. Xiao, *Phys. Rev. B* **2015**, *91*, 235425.
- [46] L. Wang, S. Tao, P. Zhu, W. Chen, *J. Mech. Des.* **2020**, *143*, 3.
- [47] P. Lyngby, K. S. Thygesen, *npj Comput. Mater.* **2022**, *8*, 232.
- [48] H. Moustafa, P. M. Lyngby, J. J. Mortensen, K. S. Thygesen, K. W. Jacobsen, *Phys. Rev. Mater.* **2023**, *7*, 14007.
- [49] M. Aykol, S. S. Dwaraknath, W. Sun, K. A. Persson, *Sci. Adv.* **2018**, *4*, eaaq0148.
- [50] W. Sun, S. T. Dacek, S. P. Ong, G. Hautier, A. Jain, W. D. Richards, A. C. Gamst, K. A. Persson, G. Ceder, *Sci. Adv.* **2016**, *2*, e1600225.
- [51] G. Kresse, J. Hafner, *Phys. Rev. B* **1993**, *47*, 558.
- [52] G. Kresse, J. Furthm  ller, *Comput. Mater. Sci.* **1996**, *6*, 15.
- [53] A. Togo, I. Tanaka, *Scr. Mater.* **2015**, *108*, 1.
- [54] A. P. Bart  k, R. Kondor, G. Cs  nyi, *Phys. Rev. B* **2013**, *87*, 184115.
- [55] R. Tibshirani, G. James, D. Witten, T. Hastie, *An Introduction to Statistical Learning-with Applications in R*, Springer, Berlin **2013**.
- [56] A. Gisbrecht, A. Schulz, B. Hammer, *Neurocomputing* **2015**, *147*, 71.